Sensitivity of Northern Hemisphere Extratropical Cyclone Properties to Atmospheric Resolution in the GFDL SPEAR Model

JAEYEON LEE,[a] XIAOSONG YANG,[b] EDMUND K. M. CHANG,[c] HIROYUKI MURAKAMI,[b] WILLIAM F. COOKE,[b]

[a] *Atmospheric and Oceanic Sciences Program, Princeton University, Princeton, New Jersey*

[b] *National Oceanic and Atmospheric Administration/Geophysical Fluid Dynamics Laboratory, Princeton, New Jersey*

[c] *School of Marine and Atmospheric Sciences, Stony Brook University, Stony Brook, New York*

Corresponding author: Jaeyeon Lee, jl8071@princeton.edu

Early Online Release: This preliminary version has been accepted for publication in *Journal of Climate*, may be fully cited, and has been assigned DOI 10.1175/JCLI-D-24-0770.1. The final typeset copyedited article will replace the EOR at the above DOI when it is published.

ABSTRACT

Extratropical cyclones (ETCs) significantly influence midlatitude weather and climate through their roles in transporting heat, moisture, and momentum. Accurately simulating ETCs in global climate models (GCMs) is essential for reliable weather forecasts and climate predictions/projections. Previous studies have shown that increasing the horizontal resolution of GCMs can enhance the representation of ETC characteristics. However, the impact of atmospheric resolution finer than 100 km on ETC genesis and frequency, especially when considering the effects of post-processing spectral truncation during cyclone tracking (e.g., T42 or T63), remains underexplored. This study addresses these gaps by examining the sensitivity of Northern Hemisphere ETCs to atmospheric resolutions of 100 km, 50 km, and 25 km using the fully coupled GFDL SPEAR model. Cyclone tracking is performed at spectral truncations of T42, T63, and T106 to assess the effects of spectral smoothing. Results reveal that increasing atmospheric resolution has minimal impact on the frequency of large-sized ETCs but leads to a substantial increase in the frequency of small-sized ETCs, particularly over the North Pacific and the North Atlantic. The size-dependent sensitivity of ETCs to atmospheric resolution is the most pronounced at T106, and further analyses suggest that the genesis of these small-sized ETCs are highly impacted by diabatic heating. Comparisons with various reanalysis datasets suggest that high-resolution models are likely better at capturing small-sized ETCs rather than overestimating their frequency. These findings highlight the critical importance of considering size-dependent sensitivities when interpreting ETC biases in high-resolution model outputs compared to reanalysis data and underscore the potential role of diabatic heating in genesis of small-sized ETCs.

SIGNIFICANCE STATEMENT

This study examines the impact of atmospheric resolution on simulations of extratropical cyclones, which are critical to midlatitude weather and climate. The results reveal that higher resolution minimally affects large-sized cyclone frequencies, but leads to an increase in the number of small-sized cyclone detected, particularly over oceanic regions. Although this increased detection can exaggerate existing frequency biases, it leads to an improved representation of cyclones across regions such as central Europe and Asia. Further analysis suggests that the genesis of these small-sized systems is strongly influenced by diabatic

Accepted for publication in *Journal of Climate.* DOI 10.1175/JCLI-D-24-0770.1.

heating, underscoring its potential role in high-resolution simulations. These findings highlight the importance of carefully considering cyclone size dependence, model resolution, diabatic processes when interpreting cyclone bias in high-resolution models.

1. Introduction

Extratropical cyclones (ETCs) are important midlatitude weather systems that play a crucial role in the general circulation. They act as a conduit for transferring heat, momentum, and moisture between low and high latitudes (Chang et al., 2002; Kaspi & Schneider, 2013). ETCs are responsible for a large portion of mid-latitude mean and extreme precipitation (Hawcroft et al., 2012; Catto & Pfahl, 2013) and frequently cause extreme surface winds (Earl et al., 2017; Hart et al., 2017), particularly during the winter season.

Global Climate Models (GCMs) have been widely employed to study the climatology and characteristics of ETCs. Although modern GCMs from the fifth and sixth phases of the Climate Model Intercomparison Project (CMIP5/CMIP6) have been able to capture the general features of storm tracks, they still exhibit biases in the magnitude and spatial distribution of regional storm tracks (Pinto et al., 2013; Christensen et al., 2013; Priestley et al., 2020a). Specifically, CMIP5/CMIP6 models often displace wintertime ETCs too far equatorward over the North Pacific and extend them excessively into Europe from the North Atlantic (Chang et al., 2012; Chang, 2013; Harvey et al., 2020; Priestley et al., 2020).

Previous studies have suggested a possible link between model resolution and the representation of ETCs (Zappa et al., 2013; Colle et al., 2013; Seiler & Zwiers, 2016; Priestley et al., 2020a; Priestley & Catto, 2022). Although atmospheric resolutions from 100 km to 250 km are too coarse to resolve mesoscale ETC features effectively (Willison et al., 2013), increasing model resolution from 250 km to 100 km has been shown to reduce ETC frequency bias (Zappa et al., 2013; Colle et al., 2013; Seiler & Zwiers, 2016; Priestley et al., 2020a). However, the impact of further increasing resolution from 100 km to 25 km is not well understood. Recent efforts using HighResMIP models with 25–50 km resolution (Haarsma et al., 2020) demonstrate that higher-resolution can enhance the representation of the ETC structure. However, the increased resolution has a marginal impact on the spatial distribution of ETCs (Priestley & Catto, 2022). This limited sensitivity may partly result from spectrally truncating field at T42 or T63, which can obscure small-scale features during cyclone tracking (Jung et al. 2006). In addition, the results from the HighResMIP models could be influenced by different model physics. Accordingly, despite these efforts, identifying the sensitivity of ETCs, particularly regarding spectral truncation effects and size-dependent cyclone characteristics, to increasing atmospheric model resolution remains a challenge.

This study aims to address this gap by evaluating the impact of atmospheric resolution change on the characteristics and geographical distribution of ETCs using the Seamless system for Prediction and EArth system Research (SPEAR) model (Delworth et al., 2020), which is a fully coupled model developed by the Geophysical Fluid Dynamics Laboratory (GFDL). ETCs are tracked at various spectral truncations (T42, T63, and T106) to assess their sensitivity to atmospheric resolution changes. Spectral wavenumber truncation, which removes noise and planetary waves, is needed to apply the Lagrangian ETC tracking method (Hoskins and Hodges, 2002). Since spectral truncation could influence the frequency of ETCs tracked by automated algorithms (Blender and Schuber, 2000) and the representation of small-scale developments of ETCs, such as secondary cyclogenesis (Rohrer et al., 2020), an appropriate spectral truncation is important for accurately capturing ETC properties and their sensitivity to atmosphere resolution change. The limited difference in ETC frequencies across resolution in previous studies may be related to their low spectral truncation wavenumbers (e.g., T42 and T63). Therefore, we aim to investigate 1) how ETC frequency sensitivity to atmospheric resolution depends on the spectral truncation used for tracking, 2) whether this sensitivity varies by ETC horizontal size, 3) what physical mechanisms govern the distinct resolution sensitivities of large- and small-sized ETCs, and 4) how these differences inform the interpretation of model bias relative to reanalysis uncertainty.

The subsequent sections are organized as follows: Section 2 describes the model, the ETC tracking method, and the method for identifying ETC horizontal size; Section 3 describes the sensitivity of ETC frequency to atmospheric resolution and spectral truncation, examines cyclone characteristics (intensity, lifetime, and size), explores the physical mechanisms underlying the resolution sensitivities of large- and small-sized ETCs, and evaluates the role of reanalysis uncertainty in interpreting model biases; finally, Section 4 provides summary and discussion.

2. Data and Methods

a. ERA5 and SPEAR models

The six-hourly SLP data for the extended winter season (November–March) from 1991 to 2020 is obtained from ERA5, the latest atmospheric reanalysis data by the European Centre for Medium-Range Weather Forecasts (Hersbach et al., 2020). The six-hourly ERA5 is considered as the reference data for comparing with SPEAR models in this study. For comparison, both ERA5 and SPEAR model outputs were remapped onto a common 1°×1° grid.

We also employ six-hourly SLP output from three different atmospheric configurations of the SPEAR model: SPEAR-LO (100 km), SPEAR-MED (50 km), and SPEAR-HI (25 km). The SPEAR model utilizes atmosphere and land components corresponding to AM4.0 and LM4.0 (Zhao et al., 2018a, b), respectively. All three versions utilize 1° horizontal resolution ocean (with refinement to ⅓° near the Equator) and sea ice components identical to MOM6 and SIS2 (Adcroft et al., 2019), respectively. This setup allows us to isolate the effects of atmospheric horizontal resolution in a coupled model. Note that throughout this study, the term 'atmospheric resolution' specifically refers to the horizontal resolution of the atmospheric component, as distinct from the oceanic resolution. Vertical resolution is not changed here. In this study, we analyze the historical simulations from 1991 to 2020 using the three SPEAR models, each comprising ten ensemble members. Further details on the models and simulations are available in Delworth et al. (2020) for SPEAR-LO and SPEAR-MED, and Jong et al. (2023; 2024) and Murakami et al. (2024) for SPEAR-HI. The SPEAR models have been extensively applied to investigate the variability and predictability of tropical cyclones (Murakami et al., 2020; 2023; 2024; Wang et al., 2023; 2024), extreme precipitation associated with tropical cyclones (Jong et al., 2023; 2024), as well as extratropical synoptic-scale phenomena, such as midlatitude baroclinic waves (Zhang et al., 2021), atmospheric rivers associated with developing ETCs (Tseng et al., 2021), and extratropical storm tracks (Yang et al., 2022).

b. ETC detection and tracking

ETCs are identified with the TRACK algorithm (Hodges, 1994; 1995; 1999), following the approach of Hoskins and Hodges (2002). To investigate the sensitivity to spectral truncation level, the algorithm is applied to spectrally truncated SLP fields at three different wavenumber truncations: T42 (~310 km), T63 (~210 km), and T106 (~125 km). Zonal wavenumbers less than five are removed to exclude the large-scale background field. The TRACK algorithm employs the connected component labeling method to identify objects on the SLP field, designate the local minimum of an object as the ETC center, and subsequently track this center. For initial tracking, the algorithm uses the nearest neighbor approach to locate the ETC at the next time step. Subsequently, the algorithm leverages the ETC information at the previous and present time steps, accounting for the ETC's propagation speed and angle, to locate the ETC in the subsequent time step. After tracking is complete, the algorithm smooths the ETC tracks through the minimization of a cost function consisting of an angle and the speed of an ETC propagation. Following Hoskins and Hodges (2002), we retain only systems that persist for at least 2 days, travel at least 1000 km, and originate north of 25°N to reduce detection of subtropical disturbances.

c. ETC effective area detector

The detected effective areas of ETCs are crucial for estimating ETC-related precipitation and surface winds (Hawcroft et al., 2012; Kang et al., 2019). Typically, an ETC's effective area is defined by a fixed effective radius determined empirically. However, due to the highly varying and complex shape of ETCs, defining their effective areas using a fixed radius may lead to misrepresentation of their actual extents. To address this issue, we choose an ETC effective area detector that considers a closed SLP contour associated with an ETC as its effective area (Wernli and Davies, 1997).

An example output from this detector, which is applied to a spectrally truncated SLP field at T42, is shown in Figure 1. The detector first identifies the SLP contour where a given ETC center is located and then searches for the outermost closed contour at a 0.2 hPa interval. If a closed contour is detected, the area within it is defined as the effective area of the given ETC. If multiple ETCs are detected within a single closed contour, the calculation is repeated until each ETC is enclosed within its own closed contour. For instance, if two ETCs are within a closed contour, the process continues until two separate closed contours are identified. If the detector fails to find separate closed contours, the detected area information is assigned to the strongest ETC. Consequently, each ETC is provided with an effective area for each time step of its lifetime.

The detected ETC's area (A) is calculated as the sum of the areas of all grid cells ($A_{unit,i}$) in the detected closed contour. The area of each grid cell depends on its specific latitude (ϕ_i):

$$\Delta x_i = 2\pi R \cos \phi_{i,rad} \cdot \frac{\Delta\lambda}{360} \tag{1}$$

$$\Delta y = 2\pi R \cdot \frac{\Delta\phi}{360} \tag{2}$$

where R = 6,371 km is the Earth's radius, $\phi_{i,rad}$ is the latitude (in radians) of the i-th grid point within the detected closed contour, $\Delta\lambda$ and $\Delta\phi$ are the grid spacings in longitude and latitude. The area of an individual grid cell ($A_{unit,i}$) and ETC's area (A) are then given by:

$$A_{unit,i} = \Delta x_i \cdot \Delta y \tag{3}$$

$$A = \sum_{i=1}^{N} A_{unit,i} \tag{4}$$

Here, N represents the total number of grid cells enclosed within the detected closed contour of the ETC. As suggested by Rudeva and Gulev (2007), the effective radius (R_e) of each ETC, assuming a circular shape, is calculated as:

$$R_e = \sqrt{A/\boldsymbol{\pi}} \tag{5}$$

This approach simplifies and quantifies ETC size by attributing its complex geometry to an equivalent circular area. The effective radius is used to classify the size of ETCs that are sensitive to model atmospheric resolution.

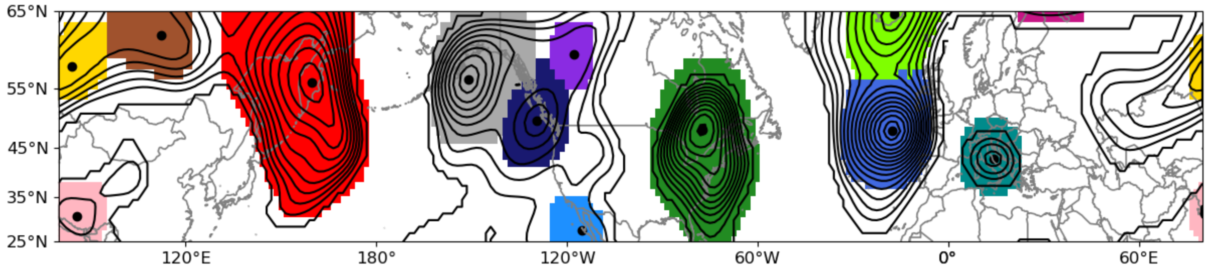

Fig. 1. An example output from the ETC effective area detector for November 24, 1991, at 18:00 UTC, using the ERA5 dataset. The contours represent truncated T42 SLP associated with ETCs, while the shaded regions indicate the detected ETC effective areas. Black dots denote the centers of the detected ETCs.

Accepted for publication in *Journal of Climate*. DOI 10.1175/JCLI-D-24-0770.1.

d. SOM analysis for small-sized ETC formation classification

We apply the Self-Organizing Map (SOM) algorithm (Kohonen, 2001) to objectively classify and analyze distinct spatial patterns associated with small-sized ETC formation. SOM is an unsupervised neural network technique widely used in atmospheric sciences that reduces high-dimensional data into a low-dimensional array of nodes based on Euclidean distance through iterative training (Kohonen, 2001, 2013). The SOM method accommodates nonlinearities within datasets without assuming orthogonality between clusters (Reusch et al., 2005) and does not require prior assumptions or knowledge of expected results, thus ensuring an objective classification.

In this study, we specifically focused on very small-sized ETCs (effective radius ≤ 600 km) identified in two regions highly sensitive to atmospheric resolution changes: the North Pacific (153–210°E, 30–45°N) and the North Atlantic (320–360°E, 50–65°N). We first extracted small-sized ETC events occurring within these domains. Instantaneous fields of SLP, ±20° in latitude and longitude around each cyclone center at cyclone genesis time, were prepared and then used to train the SOM. Through multiple sensitivity tests varying node arrangements systematically, we found a 4×2 (eight nodes) array to be optimal for clearly distinguishing and extracting the complex spatial patterns associated with small-sized cyclogenesis, while maintaining interpretability. Other parameters follow the suggestions of Li et al. (2024).

3. Results

a. Sensitivity of ETC frequency to atmospheric resolution and truncation

To establish how ETC frequency responds to atmospheric resolution and spectral truncation, we first assess ETC frequencies in the Northern Hemisphere (NH) using the ERA5 data spectrally truncated at T42, T63, and T106 to examine the impact of various spectral truncation numbers on the detection of ETCs (Figure 2). Following the approach of Hoskins and Hodges (2002), ETC frequency is defined as the count of ETCs passing within the 555-km radius of a grid point, with each ETC being counted only once at each grid point. In Figure 2d, a two-sample, two-tailed t-test ($p < 0.05$) is performed at each grid point using annual T42 and T106 ETC frequency over 29 winters to highlight where T42 and T106 differ significantly. ERA5 exhibits consistent spatial distributions of the extended winter NH ETC frequencies across T42, T63, and T106 (Figures 2a–c), with high oceanic ETC frequencies over the North Pacific and the North Atlantic, and high continental ETC frequencies over regions downstream of the Altai-Sayan Mountains, the Tibetan Plateau, and the Rocky Mountains. However, there are clear quantitative differences in ETC frequencies across different spectral truncations. The most pronounced differences of ETC frequencies between T106 and T42 occur in the regions with high oceanic and continental ETC frequencies (Figure 2d), particularly along the Kuroshio-Oyashio Extension, where the T106 ETC frequency is approximately 60% higher than that at T42. Overall, the total number of detected ETC centers per month increases with the truncation wavenumber, with T106 identifying 4206.6 ETCs, T63 identifying 3261.4 ETCs, and T42 identifying 2472.4 ETCs across the NH (Table 1). This sensitivity of quantity and geographical distribution of ETC frequency to spectral truncation wavenumber aligns with previous findings that higher spectral truncation wavenumbers lead to more detected ETCs (Blender and Schuber, 2000; Jung et al., 2006).

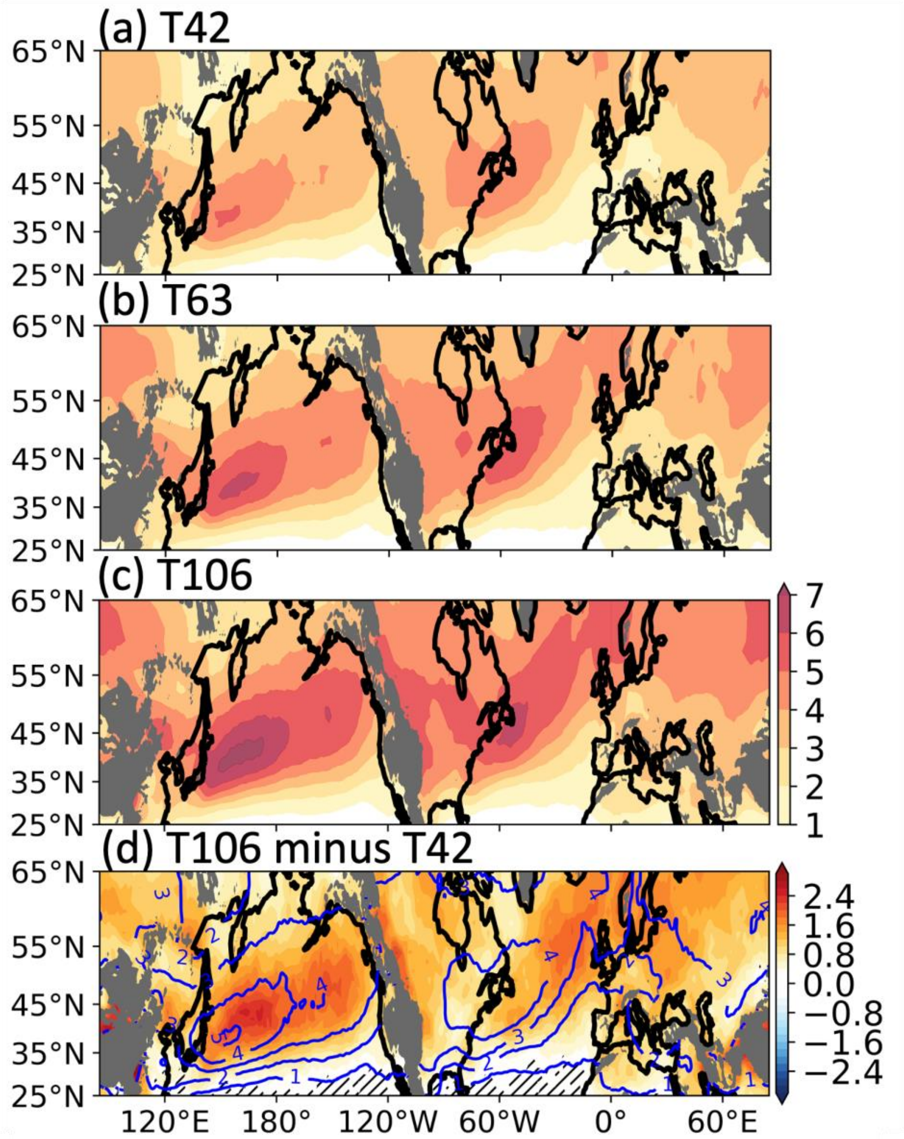

Fig. 2. Geographical distributions of ETC frequencies (shadings; in #/month) in the Northern Hemisphere at (a) T42, (b) T63, and (c) T106 spectral resolutions, and (d) the difference of ETC frequencies between T106 and T42 in ERA5. Non-significant differences ($p \geq 0.05$) determined via t-tests at each grid point are overlaid with hatching. Blue contours in (d) represent the T42 ETC frequency pattern, while gray-shaded areas indicate regions of high terrain exceeding 1,000 m in altitude. The unit is # per month.

Name	T42 ETCs	T63 ETCs	T106 ETCs
ERA5	2472.4	3261.4	4206.6
SPEAR-LO	2383.9±16.6	3168.3±21.6	4068.3±20.7

Accepted for publication in *Journal of Climate.* DOI 10.1175/JCLI-D-24-0770.1.

SPEAR-MED	2440.0±15.4	3259.5±18.7	4302.6±27.0
SPEAR-HI	2450.8±15.3	3289.9±21.4	4442.3±22.7

Table 1. Number of detected ETCs per month in ERA5 and the ensemble mean from SPEAR models, including standard deviations, over 30 extended winter seasons (November–March, 1991–2020).

The sensitivities of ETC frequency biases at T42, T63, and T106 to atmospheric resolution changes in the SPEAR models are investigated (Figure 3). To assess inter-member consistency, we quantify the percentage of ensemble members agreeing on the sign of the model bias. This ensemble consensus metric is applied to Figures 3, 4, 7–10 to reflect the robustness of the model bias. Despite quantitative differences across truncation levels, the SPEAR models show robust spatial patterns in ETC frequency bias. For instance, the peaks in ETC frequencies over the North Pacific and North Atlantic are underestimated at all truncations. Conversely, ETC frequencies in the southern parts of downstream regions of these high oceanic ETC frequencies are overestimated, especially at higher wavenumber truncations (shadings in Figures 3).

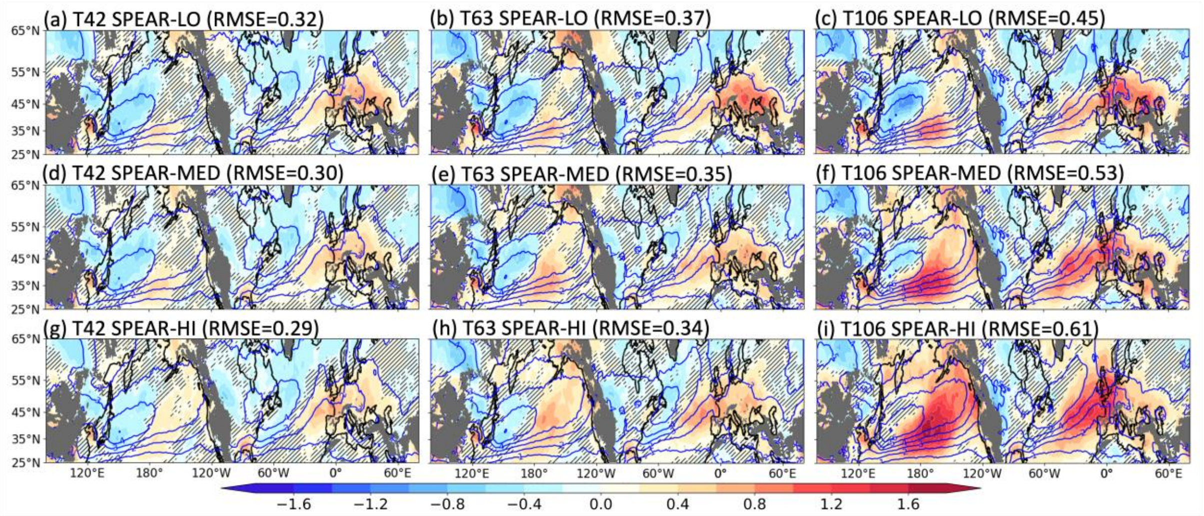

Fig. 3. Differences in ETC frequency between (a, d, g) T42, (b, e, h) T63, and (c, f, i) T106 for (top) SPEAR-LO, (middle) SPEAR-MED, and (bottom) SPEAR-HI compared to ERA5. Shading indicates ETC frequency bias relative to ERA5. Blue contours show the ETC frequency climatology in ERA5. Root-mean-square error (RMSE) listed. Gray shadings

Accepted for publication in *Journal of Climate.* DOI 10.1175/JCLI-D-24-0770.1.

indicate topography over 1,000 meters in altitude. Hatched areas denote regions where fewer than 10% of the ensemble members agree. The unit is # per month.

The sensitivity of ETC frequency biases in SPEAR to atmospheric resolution varies across truncation wavenumbers. The T42 ETC frequency bias shows weak improvement, with RMSE decreasing from 0.32 in SPEAR-LO to 0.29 in SPEAR-HI (Figures 3a, 3d, and 3g). Specifically, while higher atmospheric resolution improves the representation of ETC frequencies in the western and central North Pacific, Asian continent, and central Europe, slightly increased biases are observed over North America and its offshore areas, the eastern North Atlantic, and western Europe (Figures 3a, 3d, and 3g). These biases in ETC frequency are mostly due to an underestimation of cyclogenesis, which is defined as the location of ETC at the initial time step, near the upstream regions of the North Pacific and North Atlantic storm tracks (Chang et al., 2002; Hoskins and Hodges, 2002), and an overestimation of cyclogenesis in downstream regions (Figure 4). Despite these biases, the overall pattern of T42 ETC frequency biases remains consistent across SPEAR-LO, SPEAR-MED, and SPEAR-HI. The T63 ETC frequency bias shows a similar weak improvement, with RMSE slightly decreasing from 0.37 to 0.34 (Figures 3b, 3e, and 3h). These weak sensitivities are consistent with those in HiResMIP models (Priestley & Catto, 2022).

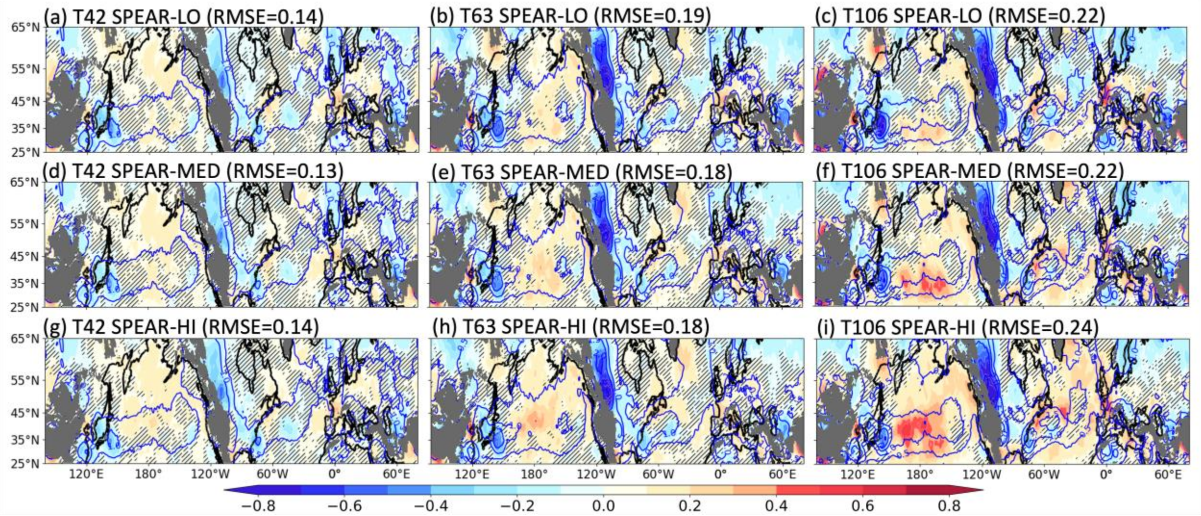

Fig. 4. Same as Figure 3 but for cyclogenesis.

In contrast, the T106 ETC frequency biases show a more pronounced sensitivity to atmospheric resolution than T42 and T63, with RMSE increasing from 0.45 in SPEAR-LO to 0.61 in SPEAR-HI. In regions such as central Europe and Asia, biases are reduced at higher resolutions, similar to T42 and T63 (Figures 3c, 3f, and 3i). However, the biases display strong sensitivity to atmospheric resolution over the ocean (e.g., the North Pacific and the North Atlantic). The underestimation of ETC frequency in regions with high ETC frequency climatology is reduced, while the overestimation of ETC frequency in downstream regions is notably enhanced in SPEAR-MED and SPEAR-HI. This resolution sensitivity is also reflected in cyclogenesis bias, with reduced bias in cyclogenesis regions near storm track entrances and increased bias in downstream regions (Figure 4). This key result highlights that while the sensitivity of ETC frequency to atmospheric resolution is modest at T42 and T63, it becomes substantially more pronounced at T106. This suggests that higher truncation in T106 enables the detection of ETC properties that are more sensitive to atmospheric resolution, possibly linked to cyclone size.

b. The dominant role of cyclone size in resolution sensitivity

To better understand the characteristics of increased oceanic ETCs at higher atmospheric resolutions, we analyze how resolution affects key cyclone characteristics, especially size (measured by effective radius), but also their maximum intensity and lifetime (Figure 5). In this study, cyclone intensity is defined as the minimum central SLP anomaly along the track, and cyclone lifetime is calculated as the number of 6-hourly time steps for which the cyclone is continuously tracked. This analysis focuses on ETCs passing through the North Pacific (30–60°N, 145–235°E) and the North Atlantic (30–70°N, 290–360°E) regions.

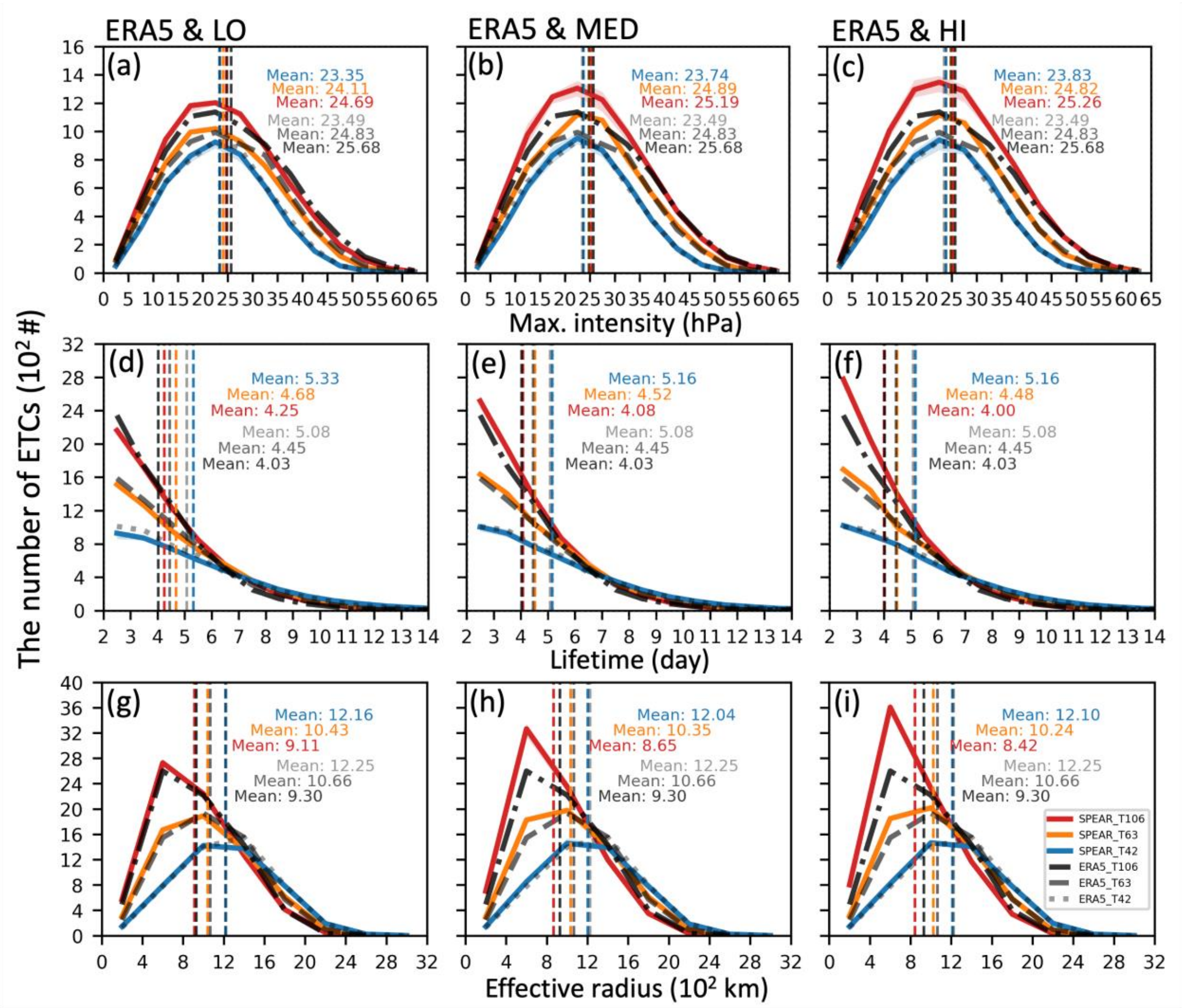

Fig. 5. Distributions of (a–c) maximum intensity (in hPa), (d–f) lifetime (in days), and (g–i) effective radius (in 10^2 km) for oceanic ETCs in ERA5 (dotted black lines) and SPEAR models (colored lines). Maximum intensity is defined as the absolute value of the lowest central SLP anomaly (in hPa) so that higher values represent stronger ETCs. Note that these values represent SLP anomalies, not absolute SLP values. The three columns correspond to SPEAR-LO (first column), SPEAR-MED (second column), and SPEAR-HI (third column) with T42 (blue), T63 (orange), and T106 (red). Bright shadings mean the ensemble spread of each model. Vertical dashed lines denote the mean value of each distribution.

SPEAR-LO tends to overestimate the frequency of relatively weak ETCs while underestimating the occurrence of strongly intensified ETCs (maximum intensity ≥ 22 hPa) across all three truncation numbers (T42, T63, and T106). This tendency is reflected in the lower mean maximum intensity values in SPEAR-LO–23.35 hPa, 23.96 hPa, and 24.69 hPa

Accepted for publication in *Journal of Climate.* DOI 10.1175/JCLI-D-24-0770.1.

for T42, T63, and T106, respectively–compared to the corresponding ERA5 mean values of 23.57 hPa, 24.52 hPa, and 25.69 hPa, respectively (compare black and colored lines in Figure 5a). The underestimation of strongly intensified ETCs is mitigated with increasing atmospheric resolution. In SPEAR-MED and SPEAR-HI, higher mean values for maximum intensity are observed, with SPEAR-MED showing 23.74/24.38/25.19 hPa and SPEAR-HI yielding 23.83/24.58/25.26 hPa at T42/T63/T106 resolutions, respectively (Figures 5b and 5c). These values are more aligned with ERA5, indicating that increasing atmospheric resolution reduces the underestimation of strongly intensified ETCs in SPEAR-LO.

This result aligns with previous findings that higher-resolution models tend to simulate more intense ETCs (Willison et al., 2013; Jiaxiang et al., 2020; Priestley and Catto, 2022). While this improvement in representing strongly intensified ETCs at higher resolutions is noticeable, it is also accompanied by an increased frequency of weakly intensified ETCs. Higher atmospheric resolution tends to result in increased detection of weaker ETCs, leading to a higher overall number of ETCs, particularly in SPEAR-MED and SPEAR-HI. It is consistent with expectations that higher-resolution models can resolve more detailed structures, potentially leading to more frequent detection of weaker ETCs, possibly due to the cyclone detection thresholds being exceeded more frequently (Rohrer et al., 2020). Importantly, although both strongly and weakly intensified ETCs show a clear change to increased atmospheric resolution, the increase in mean maximum intensity with atmospheric resolution suggests that strongly intensified ETCs are more sensitive to changes in atmospheric resolution than weakly intensified ETCs. This sensitivity is particularly pronounced at higher wavenumber truncations.

Regarding ETC lifetime distribution, SPEAR-LO tends to underestimate the short-lived ETCs (lifetime < 4 days) while overestimating the long-lived ones (lifetime ≥ 4 days) across all truncation wavenumbers (Figures 5e and 5f). Interestingly, a higher wavenumber truncation leads to increased detection of short-lived ETCs, while it also decreases the detection of long-lived ETCs. This result aligns with previous findings (e.g., Jung et al., 2006; Rohrer et al., 2020). Rohrer et al. (2020) reported that increased short-lived ETCs in reanalysis at higher wavenumber truncations might indicate more detection of ETC splitting, such as secondary cyclogenesis, as ETC splitting into two systems is often misrepresented as one at lower wavenumber truncations. This tendency is reflected in the longer mean lifetimes observed in SPEAR-LO, with respective mean values of 5.33/4.60/4.25 days at

Accepted for publication in *Journal of Climate.* DOI 10.1175/JCLI-D-24-0770.1.

T42/T63/T106, compared to ERA5's mean values of 5.11/4.30/4.03 days. SPEAR-MED and SPEAR-HI detect more short-lived ETCs, while showing similar long-lived ETCs compared to SPEAR-LO, with mean lifetimes of 5.16/4.45/4.08 days in SPEAR-MED and 5.16/4.41/4.00 days in SPEAR-HI, aligning more closely with ERA5 (Figures 5g and 5h). The results suggest that higher atmospheric resolution results in more frequent detection of short-lived ETCs, alleviating the underestimations in SPEAR-LO. However, while higher atmospheric resolution could improve the distribution of the mean lifetime in SPEAR models, it also leads to overestimating the overall frequency of short-lived ETCs. This feature is particularly evident in ETCs at the higher wavenumber truncation, which are more sensitive to changes in atmospheric resolution compared to the lower wavenumber truncation. This finding suggests that higher atmospheric resolution may improve the representation of the mean lifetime distribution, indicating that the overestimation is not just limited to short-lived ETCs but also to long-lived ETCs.

For the ETC effective radii across T42, T63, and T106, SPEAR-LO slightly underestimates the occurrence of large-sized ETCs (effective radius ≥ 1,200 km) while largely overestimating small-sized ETCs (effective radius < 1,200 km), resulting in mean effective radii of 1,216/1,043/911 km, respectively, compared to ERA5's mean values of 1,225/1,066/930 km. This tendency to overestimate small-sized ETCs becomes more pronounced at higher truncation wavenumbers, with the frequency of small-sized ETCs increasing with higher atmospheric resolutions (Figures 5i–l). Conversely, while large-sized ETCs tend to be somewhat underestimated, their sensitivity to changes in atmospheric resolution is notably less pronounced. At T42, the SPEAR models exhibit very weak sensitivity to changes in atmospheric resolution, with only slight reductions in the underestimation of large-sized ETCs and a minor increase in small-sized ETCs in SPEAR-MED and SPEAR-HI, yielding mean values of 1,240 km and 1,210 km, respectively. At T63, the higher atmospheric resolutions in the SPEAR models lead to a further decrease in the mean effective radius from 1,043 km to 1,024 km. This change is mainly due to an increase in small-sized ETC occurrences, while the reduction in large-sized ETCs is relatively less pronounced. It becomes even more pronounced at T106, where the mean effective radius declines from 911 km to 842 km, with SPEAR-HI showing a substantial reduction compared to ERA5's mean value of 930 km. These findings suggest that as atmospheric resolution increases, the SPEAR models disproportionately capture more small-sized ETCs, whereas the occurrence of large-sized ETCs, while slightly underestimated, exhibits weak sensitivity to further increase in atmospheric resolution. This highlights a size-dependent sensitivity, with small-sized ETCs being more sensitive to changes in atmospheric resolution than their larger counterparts.

Our results show that although small-sized ETCs tend to be short-lived, they are not necessarily weak. Correlation coefficients between size and maximum intensity for all oceanic ETCs ranges from 0.53 to 0.57 and it becomes notably weaker for small-sized ETCs (having less than 600 km effective radius; 0.21–0.25). This contrasts with the findings of Rudeva and Gulev (2007), who reported a strong positive correlation between cyclone size and intensity. Consistent with this, our joint PDFs (Figure S4) reveal that while larger ETCs generally exhibit stronger maximum intensities and longer lifetimes, a subset of small-sized systems also displays relatively high intensities despite their shorter duration. One possible explanation is that many of the small-sized ETCs identified in higher-resolution SPEAR models may originate from secondary cyclogenesis. In such cases, secondary cyclones can occasionally develop stronger intensities than their primary counterparts (Ludwig et al., 2015).

In contrast to the discrepancy in oceanic ETC characteristics across different atmospheric resolutions, characteristics of continental ETCs–those passing through Eurasia (30–65°N, 0–145°E) and North America (30–65°N, 235–290°E) domains–exhibit marginal difference across SPEAR models (Figure 6). For these continental ETCs, distributions of all characteristics generally converge, suggesting that the resolution-induced biases observed over oceans are less pronounced over the land. The SPEAR models closely match ERA5 regarding the distributions of maximum intensity, lifetime, and effective radius for continental ETCs, indicating that the models effectively capture the overall structure and lifecycle of continental ETCs across resolutions. The relatively stable frequency bias pattern observed over land (Figure 3) further supports this convergence in continental ETC characteristics, as the distributions of these characteristics tend to remain consistent regardless of resolution changes. Additionally, it is possible that partial offsetting of regional biases. For example, cyclogenesis bias is not only enhanced over the offshore regions but also reduced downstream of the Rocky Mountains, which may be associated with the impact of resolved orography (Priestley et al., 2020).

Accepted for publication in *Journal of Climate.* DOI 10.1175/JCLI-D-24-0770.1.

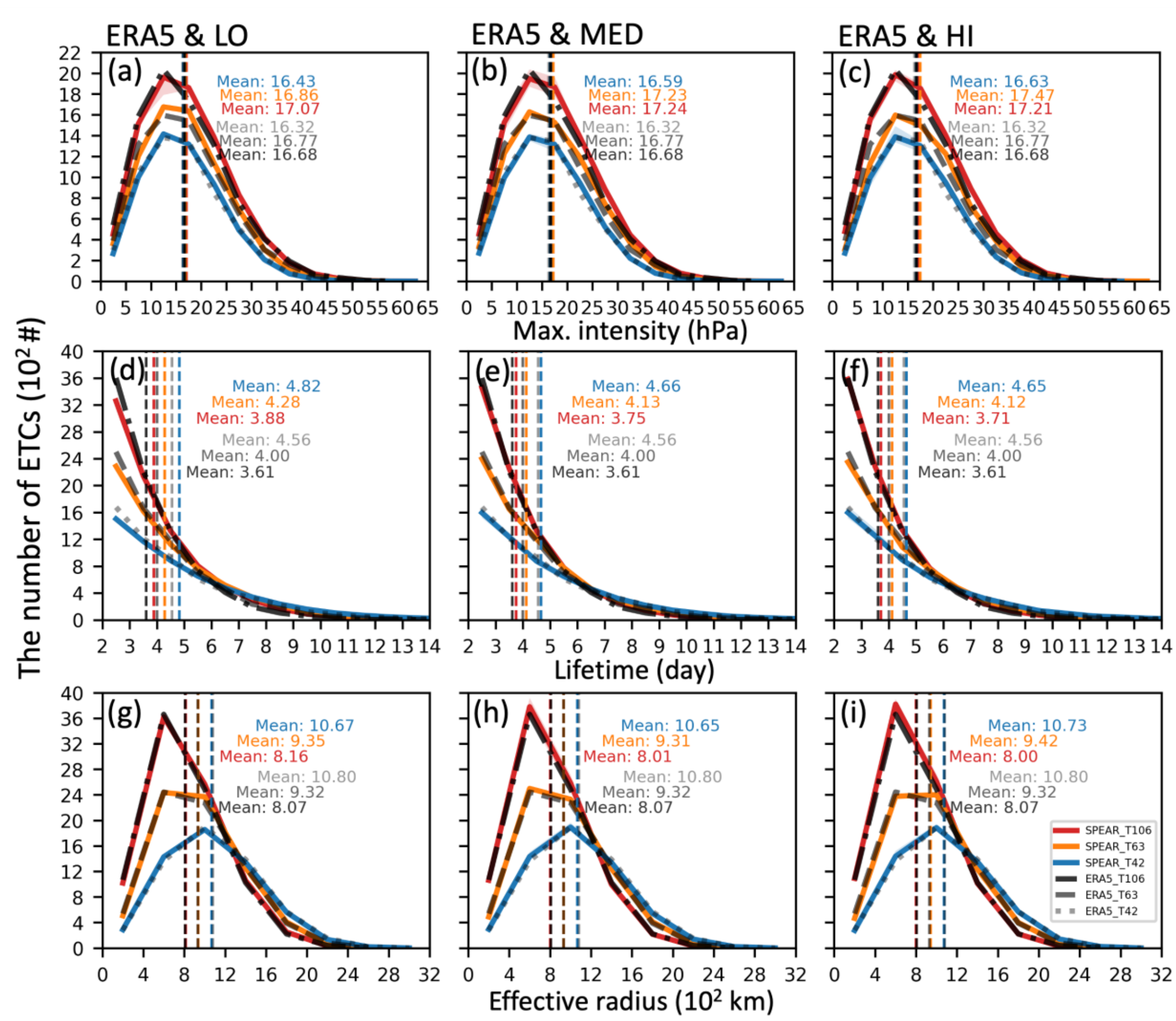

Fig. 6. Same as Figure 5 but for continental ETCs passing through Eurasia (30–65°N, 0–145°E) and North America (30–65°N, 235–290°E) domains.

To further explore the impact of atmospheric resolution changes on oceanic T106 ETCs, we examine their size-segregated frequency biases in the SPEAR simulations relative to ERA5. In both ERA5 and the SPEAR models, the effective radius distributions for different spectral truncations begin to diverge at approximately 1,200 km (Figures 5g–i); Thus, we classify ETCs into large- and small-sized categories based on this threshold. Figures 7 and 8 present biases in frequency and genesis location, respectively, for large- and small-sized ETCs tracked at T106.

In ERA5, large-sized ETCs predominantly form along the western boundaries of the North Pacific and the North Atlantic–regions characterized by strong sea surface temperature (SST) gradients–and typically propagate in the northeast direction (contours in Figures 7a and

Accepted for publication in *Journal of Climate.* DOI 10.1175/JCLI-D-24-0770.1.

8a). These regions align with the peaks of ETC frequency over the oceans, consistent with the previous findings that large-sized ETCs generally propagate along major storm tracks (Rudeva and Gulev, 2006). In the SPEAR models, the frequency of large-sized ETCs is generally underestimated over the main storm track regions, with underestimated main cyclogenesis along the western boundaries of oceans in their upstream regions (Figures 7 and 8). This large-sized ETC frequency bias is similar to bomb cyclone frequency bias (Priestley et al., 2020), highlighting the relationship between size and intensity for large-sized ETCs found in Rudeva and Gulev (2007). In downstream regions, this underestimation of large-sized ETC frequency shows only a slight increase with higher atmospheric resolution, with RMSE increasing slightly from 0.35 to 0.45.

In contrast, the small-sized ETCs display a notable overestimation bias across the SPEAR models, particularly over central oceanic regions. Over the North Pacific, the small-sized ETC frequency bias in SPEAR-LO is slightly underestimated to the north of the peak and overestimated to the south of it, as well as near the west coast of North America (Figure 7b). This bias arises from underestimated cyclogenesis in the main cyclogenesis regions and overestimated cyclogenesis in downstream areas, particularly in the central and eastern North Pacific (Figure 8b). Over the North Atlantic, SPEAR-LO overestimates small-sized ETC frequency south of the peak of small-sized ETC frequency. This small-sized ETC frequency bias is primarily due to large overestimations along the east coast of North America and south of major cyclogenesis regions, which not only offset the underestimation at the peak of cyclogenesis but also result in an overall overestimated ETC frequency. This indicates that, in both the North Pacific and the North Atlantic, biases in both large- and small-sized ETC frequencies contribute to the dipole patterns of total ETC frequency bias in SPEAR-LO (Figure 3c).

As atmospheric resolution increases in SPEAR-MED and SPEAR-HI, a notable increase in small-sized ETCs is observed over the central and eastern North Pacific and North Atlantic regions, along with some improvements in land areas like central Europe and Asia. This indicates that the discrepancy in ETC frequency bias at different atmospheric resolutions is primarily influenced by the increased bias in small-sized ETC frequencies with highly increasing RMSE from 0.47 to 0.88. The clear spatial difference and contrasting sensitivity between large- and small-sized ETCs support the interpretation that the total increase in ETC frequency with increasing atmospheric resolution is primarily driven by small-sized systems.

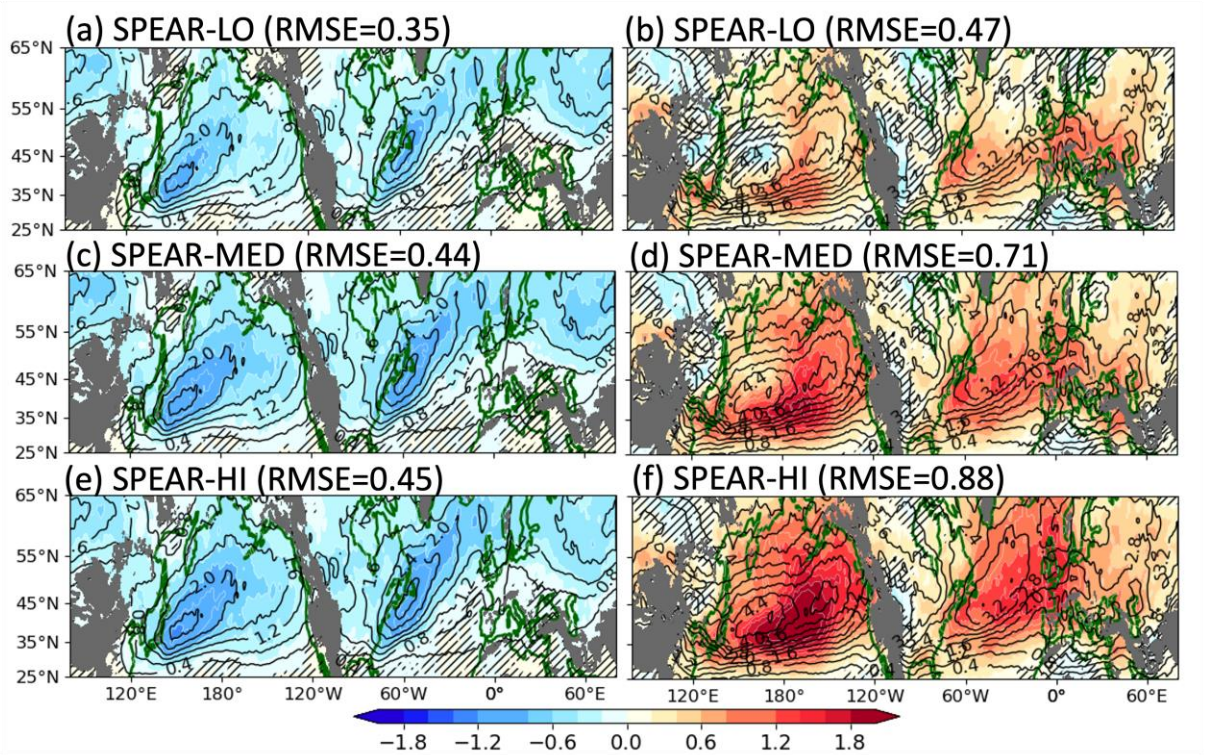

Fig. 7. Differences (shadings) in the frequencies of T106 (left column) large- and (right column) small-sized ETCs for (a, b) SPEAR-LO, (c, d) SPEAR-MED, and (e, f) SPEAR-HI compared to ERA5. Black contours indicate the ETC frequency climatology in ERA5. Root-mean-square error (RMSE) listed. Gray shadings represent topography over 1,000 meters in altitude. Hatched areas denote regions where fewer than 10% of the ensemble members agree. The unit is #/month.

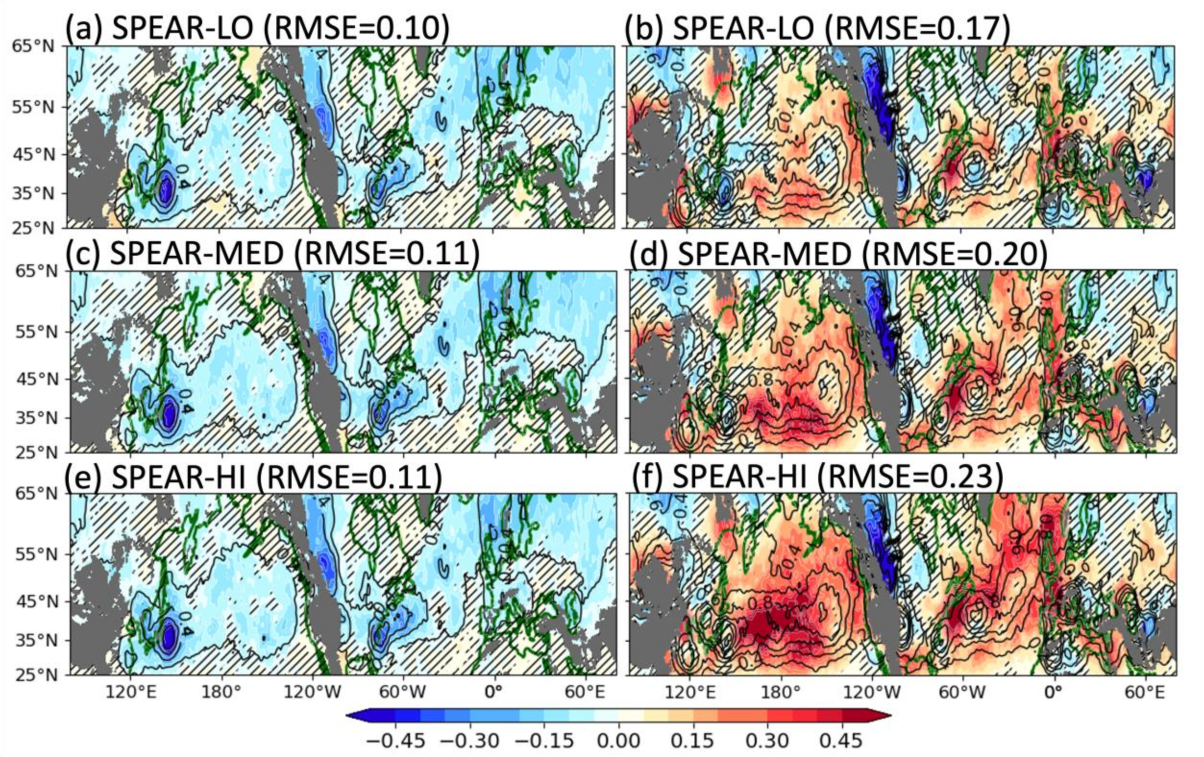

Fig. 8. Same as Figure 7, but showing the differences for (left column) large-sized and (right column) small-sized ETC genesis at T106.

c. Contrasting physical mechanisms: baroclinicity vs. diabatic processes

To understand the different sensitivities of large- and small-sized ETCs to atmospheric resolution, we examine the distinct physical mechanisms responsible for these differences. Development of ETCs is frequently attributed to baroclinic instability (Hoskins et al. 1985). The degree of instability is quantified by the maximum Eady growth rate (σ) at 700 hPa, calculated as:

$$\sigma = 0.31 f \left| \partial u / \partial z \right| N^{-1} \qquad (6)$$

where f is the Coriolis parameter, u denotes the zonal wind, and N^2 ($g \partial ln\theta / \partial z$; g is acceleration due to gravity; θ is potential temperature) represents the Brunt-Väisälä frequency squared. In SPEAR models, large-sized ETC frequency is underestimated along the strong SST gradient regions over the North Pacific and North Atlantic (Figure 7) and this underestimation is closely associated with the underestimation of baroclinicity (Figure 9), which can lead to more stable atmospheric conditions, suppressing the development of small amplitude atmospheric disturbances into ETCs. This bias in the Eady growth rate is slightly increased with increased atmospheric resolution, corresponding to the weak sensitivity in large-sized ETC frequency bias. The sensitivity of biases in both the Eady growth rate and large-sized ETC frequency to atmospheric resolution changes is related to underlying SST biases. All SPEAR models share a pronounced dipolar SST bias, with warmer north and colder south of the Kuroshio Current and the Gulf Stream, arising from the common coarse (1°) oceanic resolution (Figure 10). These SST biases weaken the low-level meridional temperature gradient, which in turn reduces wind shear and, thus, the Eady growth rate. Notably, the weakening of the meridional temperature gradient exhibits a marginal sensitivity to changes in atmospheric resolution, with only a slight increase at higher resolution. Thus, even with an identical ocean grid, differences in atmospheric resolution create atmosphere–ocean feedbacks that introduce some sensitivity in SST, but that response is very weak. This relationship underscores that the biases in large-sized ETC and associated large-sized atmospheric circulations are not sensitive to atmospheric resolution changes from 100 km to 25 km at least for the SPEAR models.

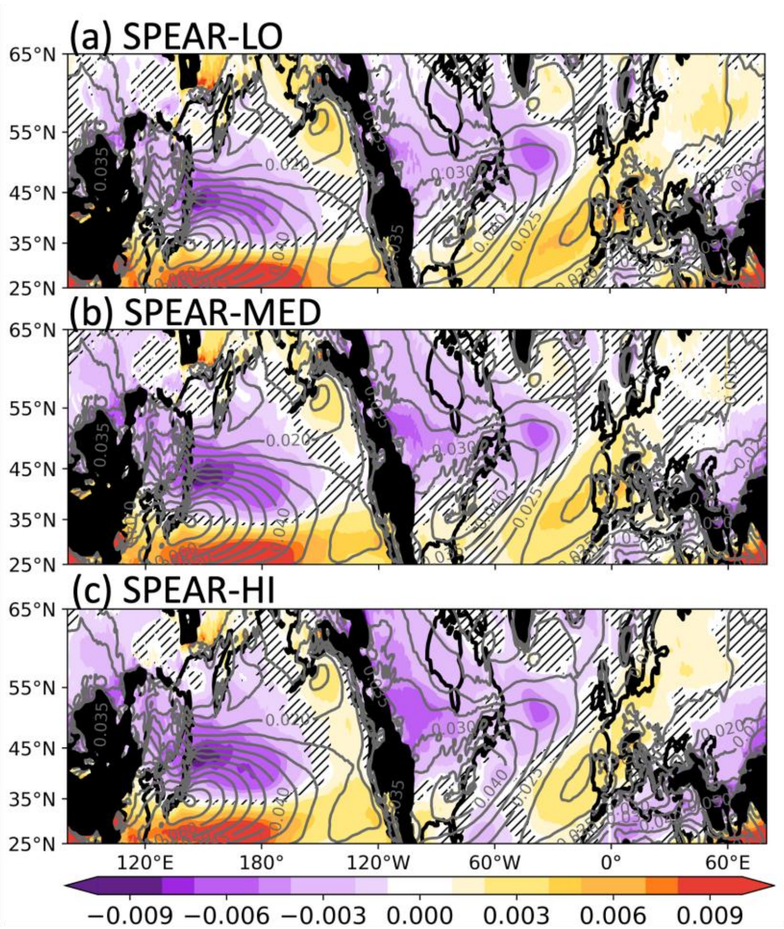

Accepted for publication in *Journal of Climate.* DOI 10.1175/JCLI-D-24-0770.1.

Fig. 9. Biases in the Eady growth rates (shadings; in day^{-1}) in the SPEAR models and climatology of the Eady growth rate (contours) in ERA5. (a), (b), and (c) represent results from SPEAR-LO, SPEAR-MED, and SPEAR-HI, respectively. Hatched areas denote regions where more than 90% of the ensemble members disagree with the sign of the ensemble mean bias. Regions with elevations above 1,000 m are masked in black.

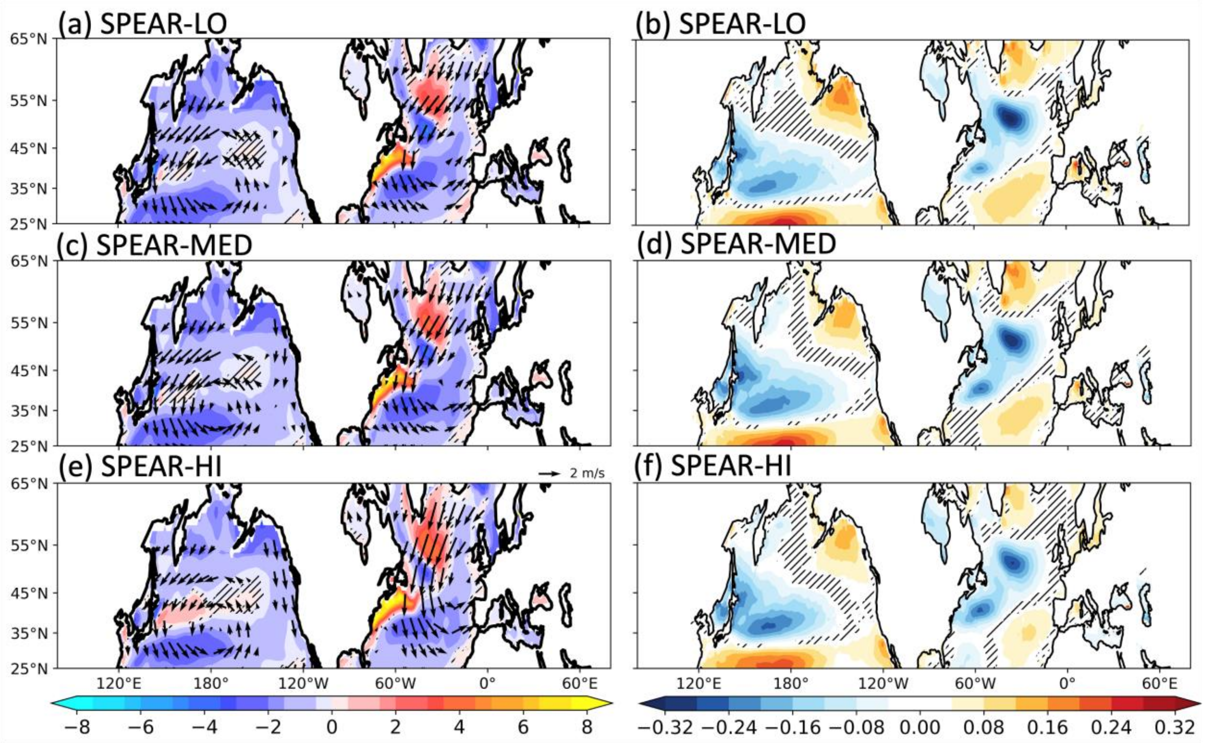

Fig. 10. Biases in (a, c, e) sea surface temperatures (shadings; in °C) with 700-hPa steering flows (black vectors; in m/s) and (b, d, f) low-level meridional potential temperature gradients (shadings; in K/degree latitude) in the SPEAR models. Hatched areas denote regions where more than 90% of the ensemble members do not agree with the ensemble mean bias. Only steering flow biases in the region, where more than 90% of the ensemble members agree, are shown. From top to bottom, the panels represent results from (a, b) SPEAR-LO, (c, d) SPEAR-MED, and (e, f) SPEAR-HI.

In contrast, small-sized ETCs increase more substantially with increasing atmospheric resolution and their behavior is not clearly linked to baroclinicity. The increased small-sized ETC frequency bias over the ocean appears to be partly driven by SST-induced low-level steering flow, which can affect the propagation of these small-sized ETCs (Figure 10). In

SPEAR models, the poleward steering flow biases emerge in regions with overestimated cyclogenesis south of peaks in the central North Pacific and the central North Atlantic, leading to more small-sized ETCs propagating poleward from lower latitude. However, the sensitivity of small-sized ETC occurrence to atmospheric resolution, which is more pronounced than in large-sized ETCs, appears distinct from the pattern of low-level baroclinicity biases.

One possible explanation for this increase in small-sized ETCs with higher resolution may be cyclone splitting, such as secondary cyclogenesis, which often occurs downstream of primary cyclone formation regions (Priestley et al., 2020b) and is influenced by finer atmospheric processes, such as frontolytic strain and strong diabatic heating (Ludwig et al., 2015; Schemm, 2023). The short lifespans and distinct geographical distributions of small-sized ETCs further support the possibility of the relationship between increased ETC frequency and secondary cyclogenesis in higher-resolution SPEAR models.

Indeed, our additional analyses using the SOM applied to composite fields of precipitation and SLP anomalies from ERA5 and SPEAR models clearly demonstrate the existence of organized precipitation patterns preceding small-sized cyclone formation (Figure 11). Such features are consistently reproduced in SPEAR models (see Figures S1–3 in supplementary material). Specifically, precipitation was evident approximately 12 hours before small-sized ETC genesis, strongly suggesting a pivotal role of diabatic heating processes in small-sized cyclogenesis. Furthermore, the SOM results (Clusters 0, 3, 4, 5, 6, and 7) indicate that most small-sized ETCs were generated via secondary cyclogenesis (about 80% of total small-sized ETCs), supporting the result that small-sized cyclones do not necessarily exhibit weaker intensity in Figure 5. Additionally, some small-sized ETCs were also found to form near high-pressure systems (Clusters 1 and 2), likely intensifying moisture transport and contributing to enhanced diabatic heating. Thus, diabatic processes and model physics at finer scales appear to play significant roles in the increased occurrence and uncertainty associated with small-sized ETCs in high-resolution SPEAR models.

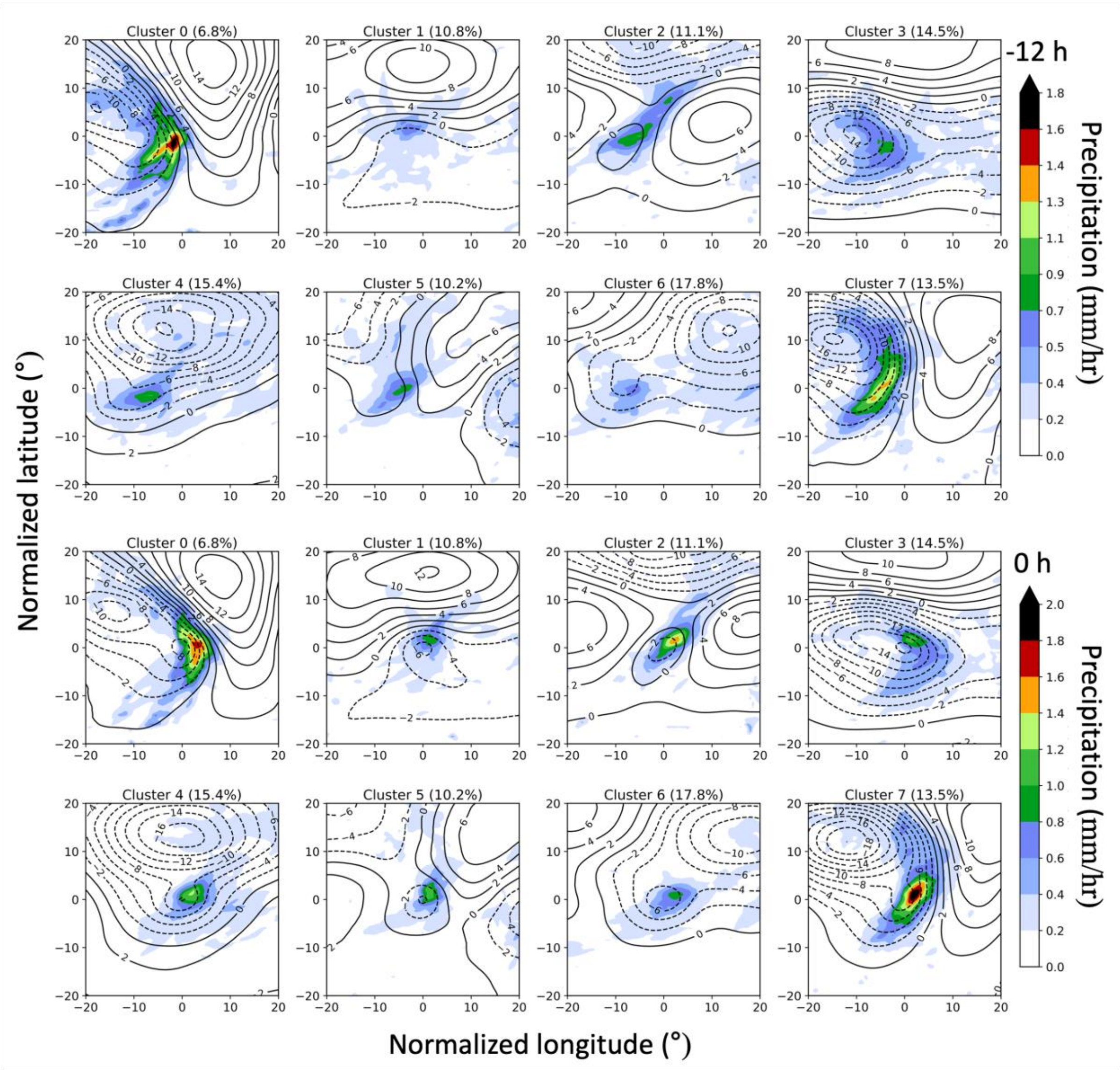

Fig. 11. Each panel shows cyclone-centered composites in ERA5 of SLP anomalies (contours; in hPa) and precipitation (shadings; in mm/hr) at the genesis time (0 h) and 12 hours before (−12 h) for T106 small-sized ETCs (effective radius ≤ 600 km), classified into eight SOM clusters (Clusters 0–7). SLP anomalies are computed relative to the six-hourly climatological mean over 1991–2020. The composites are classified using SOM. The domain of each composite field covers ±20° latitude and longitude around each cyclone center within the North Pacific (153°–210°E, 30°–45°N) and North Atlantic (320°–360°E, 50°–65°N) regions.

d. Uncertainty of reanalysis datasets for small-sized ETCs

When interpreting biases in ETCs, it is essential to account for the uncertainties in reanalysis datasets. Given the physical mechanisms underlying the increase in small-sized ETCs in high-resolution models, a key question arises: is this increase a model bias or a reflection of better detection?

Large discrepancies across different reanalysis datasets indicate that the higher frequency of small-sized ETCs in high-resolution models may not necessarily indicate an overestimation but rather reflect limitations in the representation of small-sized systems in reanalysis data (Figure 12). Higher-resolution reanalysis datasets, such as CFSR (Saha et al., 2010; Saha et al., 2014; ~38 km), ERA5 (~35 km), JRA3Q (Kosaka et al., 2024; ~40 km), tend to show a greater number of small-sized ETCs compared to lower-resolution datasets like JRA55 (Kobayashi et al., 2015; ~55 km) and MERRA2 (Gelaro et al., 2017; ~50 km). For instance, mean values for oceanic ETC effective radii are 926 km, 930 km, and 930 km for CFSR, ERA5, and JRA3Q, respectively, compared to larger mean radii of 981 km and 955 km for JRA55 and MERRA2. Additionally, the frequency of small-sized oceanic ETCs is consistently higher in CFSR, ERA5, and JRA3Q, suggesting their finer spatial resolution enhances the detection of small-sized ETCs. This tendency extends to continental ETCs, where higher-resolution datasets (e.g., CFSR, ERA5, JRA3Q) exhibit smaller mean effective radii (789–807 km) and a greater number of small-sized ETCs compared to lower-resolution datasets (816–840 km). Moreover, the discrepancy among reanalysis datasets is larger over the ocean than the land (Figures 12a and 12b), suggesting that the observational network also contributes to the uncertainty of ETCs in reanalysis datasets. The ability of higher-resolution datasets to better capture small-scale atmospheric processes, likely due to their finer spatial resolution at which their data assimilations operate (Yun et al., 2015), may play a key role in these discrepancies. In contrast, lower-resolution datasets may smooth out small-sized atmospheric processes during data assimilation, leading to a decrease in small-sized ETC frequency and an increase in mean effective radii, particularly over the oceanic regions where observational data is sparse.

These findings suggest that the apparent overestimation of small-sized ETCs in high-resolution models may partly arise from limitations in representation of small-sized ETCs in reanalysis datasets. Therefore, what is often interpreted as a model bias may instead reflect the limited ability of coarser-resolution reanalysis to capture small-sized systems.

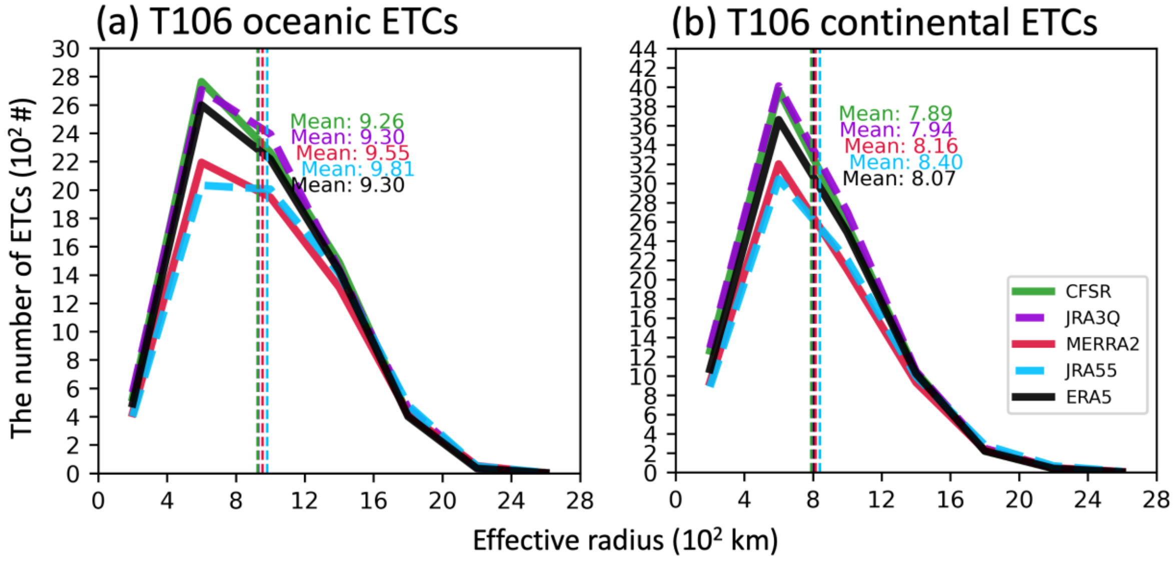

Fig. 12. Distributions of effective radius (in 10^2 km) for (a) oceanic and (b) continental T106 ETCs in ERA5 (black), JRA3Q (purple), JRA55 (blue), CFSR (green), and MERRA2 (red). Vertical dashed lines denote the mean value of each distribution.

4. Discussion and Summary

This study evaluates the sensitivity of ETCs to changes in atmospheric resolution using the GFDL SPEAR model simulations at various atmospheric model resolutions (100 km, 50 km, and 25 km) and cyclone tracking performed with SLP data at various spectral truncations (T42, T63, and T106). Key findings reveal both the benefits and challenges of interpreting biases in ETCs as atmospheric resolution increases in climate models.

Different truncations result in distinct sensitivities of ETC frequencies to atmospheric resolution changes. The T42 and T63 ETC frequencies exhibit relatively modest sensitivity, consistent with the findings in Priestley & Catto (2022). In contrast, ETC frequency at T106 demonstrates higher sensitivity. Specifically, higher atmospheric resolutions for cyclones tracked at T106 do not noticeably affect the representation of large-sized ETCs. The bias and resolution sensitivity for these large-sized ETCs are connected to the SST gradient. In contrast, high-resolution simulations tend to slightly improve small-sized continental ETCs, especially over central Europe and Asia, and largely overestimate the frequency of small-sized oceanic ETCs, especially over the North Pacific and the North Atlantic, leading to

Accepted for publication in *Journal of Climate.* DOI 10.1175/JCLI-D-24-0770.1.

increased bias in small-sized ETC frequency compared to reanalysis data. In this study, we confirm that the frequency bias of large-sized ETCs is linked to SST gradient-induced large-scale flow bias, consistent with previous findings (Woollings et al., 2010; Small et al., 2019). In contrast, the frequency of small-sized ETCs appears to be less influenced by SST biases.

The increase in ETC frequency with higher-resolution model is qualitatively consistent with earlier findings in an atmosphere-only configuration by Jung et al. (2006), suggesting the predominant impact of atmospheric resolutions despite considering atmosphere-ocean feedback. We confirmed this increase in ETC frequency is mostly contributed by the increase in small-sized ETC frequency. This sensitivity of small-sized ETC frequency likely stems from the models' increased sensitivity to mesoscale atmospheric processes, such as secondary cyclone formation, which become more pronounced at higher resolutions (Ludwig et al., 2015; Schemm, 2023). Schemm & Sprenger (2015) provide additional critical insights, highlighting that latent heat release and associated diabatic processes significantly enhance lower-tropospheric potential vorticity anomalies along fronts, facilitating frontal-wave (secondary) cyclone formation. In this study, we found that precipitation consistently occurred prior to the formation of small-sized ETCs, and approximately 90% of these systems were likely generated through secondary cyclogenesis. This suggests a strong link between diabatic processes and small-sized cyclogenesis. The improved resolution may allow the model to better resolve diabatically driven processes and along-frontal deformation fields, which could explain the substantial increase in small-sized ETC frequency observed in the higher-resolution SPEAR simulations. It is worth noting that SPEAR-HI includes additional tuning of damping and advection parameters in the dynamic core to improve simulation of tropical cyclones (Jong et al., 2023). This tuning may also contribute to the increased frequency of small-sized ETCs in SPEAR-HI compared to SPEAR-LO and -MED. Nevertheless, to better understand how increased resolution influences precipitation generation and the associated diabatic heating processes involved in small-sized cyclogenesis, future work is needed to examine how model physics—particularly those related to precipitation and latent heat release—respond to changes in atmospheric resolution.

These findings suggest that higher atmospheric resolutions still face challenges in representing small-sized ETCs, particularly over the ocean. This highlights the importance of carefully considering ETC size when using these models to investigate ETCs with mesoscale

Accepted for publication in *Journal of Climate.* DOI 10.1175/JCLI-D-24-0770.1.

features at higher truncation numbers. Additionally, small-sized ETC biases may also reflect contributions from biases in mesoscale ocean-eddy related air-sea coupling other than large-scale SST-induced baroclinicity. Because these ocean-eddy induced biases interact with the atmosphere, repeating these sensitivity tests with eddy-permitting (≤ 0.25°) oceanic resolution and with atmosphere-only runs forced by observed SST would be valuable for isolating the impact of higher oceanic resolution in further research.

Furthermore, this study emphasizes the importance of accounting for uncertainties in recent reanalysis datasets when interpreting bias in small-sized ETCs. Higher-resolution reanalysis, such as CFSR, ERA5, and JRA3Q, consistently show more frequent small-sized ETCs compared to lower-resolution datasets like JRA55 and MERRA2. The discrepancy in small-sized ETC frequency across different reanalysis datasets underscores the potential link between resolution and the representation of small-sized ETCs in reanalysis, indicating the need for caution when using reanalysis datasets as reference data for evaluating small-sized ETCs. Because of this uncertainty of small-sized ETC numbers in reanalysis datasets, the rise in small-sized ETC frequency in higher-resolution SPEAR models may not imply overestimation but instead highlight their capability to capture more small-scale processes, such as frontolytic strain and strong diabatic heating (Ludwig et al., 2015; Schemm, 2023). Nevertheless, it might reflect not only spatial resolution difference but also vertical resolution, observational inputs and data assimilation methods (Hodges et al., 2003). Thus, to further explore the relationship between model resolution and the representation of small-sized ETCs in reanalysis datasets, especially in regions with sparse in-situ observations, future analyses might benefit from Observing System Simulation Experiments (OSSEs) with high-resolution model simulations that use data from the current observing system and perform data assimilation.

Our approach, based on large-ensemble simulations using a single climate model (GFDL SPEAR), enables systematic isolation of atmospheric resolution effects on ETC representation, considering the associated atmosphere-ocean feedbacks and keeping oceanic resolutions and model physics consistent. However, it is important to note that the findings in this study reflect specific characteristics and potential biases inherent in a single model. Thus, caution should be exercised in broadly generalizing these results. Future research comparing these results with multi-model ensemble analyses could enhance the robustness of our findings by addressing inter-model variability associated with different atmospheric and oceanic physics schemes. Additionally, recent findings by Schemm (2023) suggest that convection-permitting, km-scale resolution simulations may improve ETC representation and reduce biases commonly observed at coarser resolutions. Conducting a size-dependent assessment of ETCs using convection-permitting simulations could further strengthen the conclusions drawn in this study. Furthermore, since our analysis relies on a pressure-based tracking method, the representation of ETC characteristics and spatial distributions may differ from those obtained using vorticity-based approaches (e.g., Neu et al., 2013; Hewson and Neu, 2015).

In conclusion, higher-resolution models may introduce potential overestimations of small-sized systems over the ocean, necessitating careful assessment. Given the critical role of ETCs in driving midlatitude precipitation, these biases in small-sized ETC representation could have important implications for a better understanding of midlatitude precipitation biases. These resolution sensitivities may also influence future climate projections, where enhanced latent heating and storm track shifts could further modify cyclone characteristics. Thus, understanding how model resolution affects ETCs may be important for improving confidence in future projections. Future research should focus on investigating the regional impacts of ETC biases, particularly the small-sized ETCs and their potential role in air-sea coupling processes and their potential impact on precipitation. Moreover, the ETC effective area derived from closed SLP contours may offer a physically consistent way to represent the spatial scale of surface cyclones. This measure could be useful in future studies assessing the spatial extent of wind-related impacts, such as those associated with wind footprint analyses (Gentile et al., 2023), or compound extremes involving precipitation and wind (Messmer and Simmonds, 2021). In addition, future studies could benefit from analyzing the sensitivity of ETCs to atmospheric resolution changes in the Southern Hemisphere and during Northern Hemisphere summertime, as these analyses might provide complementary insights into ETC dynamics under different baroclinic environments.

Acknowledgments.

We thank Drs. Joseph P. Clark and Marc Plange for their constructive reviews on an earlier draft and Chih-Chi Hu for his insightful comments. We are especially grateful to Editor Dr. Robert C. J. Wills for his thoughtful and supportive editorial guidance throughout the review process. We also sincerely thank Dr. Paolo De Luca and the three anonymous reviewers for their thorough and thoughtful reviews, which greatly contributed to improving the quality and clarity of the manuscript. The SOM was implemented using the Python miniSOM library (Vettigli, 2021). JL and EC acknowledge the support under award NA22OAR4310605 from the National Oceanic and Atmospheric Administration, U.S. Department of Commerce. The statements, findings, conclusions, and recommendations are those of the authors and do not necessarily reflect the views of the National Oceanic and Atmospheric Administration or the U.S. Department of Commerce.

Data Availability Statement.

The ERA5 reanalysis data is publicly available from the Copernicus Climate Data Store at https://cds.climate.copernicus.eu/. The CFSR data is available from the National Centers for Environmental Information (NCEI) at https://www.ncei.noaa.gov. The JRA-55 and JRA-3Q reanalysis datasets are provided by the Japan Meteorological Agency (JMA) and can be accessed through the JMA Climate Data Assimilation System website at https://jra.kishou.go.jp. The MERRA-2 reanalysis data are available from the NASA Goddard Earth Sciences Data and Information Services Center (GES DISC) at https://disc.gsfc.nasa.gov. SPEAR model outputs used in this study are available at https://www.gfdl.noaa.gov/spear/.

REFERENCES

Adcroft, A., and Coauthors, 2019: The GFDL global ocean and sea ice model OM4. 0: Model description and simulation features. *J. Adv. Model. Earth Syst.*, **11(10)**, 3167-3211, https://doi.org/10.1029/2019MS001726.

Blender, R., and Schubert, M., 2000: Cyclone tracking in different spatial and temporal resolutions. *Mon. Wea. Rev.*, **128(2)**, 377-384, https://doi.org/10.1175/1520-0493(2000)128<0377:CTIDSA>2.0.CO;2.

Catto, J. L., and Pfahl, S., 2013: The importance of fronts for extreme precipitation. *J. Geophys. Res.: Atmos.*, **118(19)**, 10-791, https://doi.org/10.1002/jgrd.50852.

Chang, E. K., Lee, S. and Swanson, K. L., 2002: Storm track dynamics, *J. Climate.*, **15**, 2163-2183, https://doi.org/10.1175/1520-0442(2002)015<02163:STD>2.0.CO;2.

Accepted for publication in *Journal of Climate.* DOI 10.1175/JCLI-D-24-0770.1.

Chang, E. K., Guo, Y., and Xia, X., 2012: CMIP5 multimodel ensemble projection of storm track change under global warming. *J. Geophys. Res.: Atmos.*, **117(D23)**, https://doi.org/10.1029/2012JD018578.

Chang, E. K., 2013: CMIP5 projection of significant reduction in extratropical cyclone activity over North America. *J. Climate*, **26(24)**, 9903-9922, https://doi.org/10.1175/JCLI-D-13-00209.1.

Christensen, J. H., and Coauthors, 2013: Climate phenomena and their relevance for future regional climate change. *Climate Change 2013: The Physical Science Basis*, TF Stocker et al., Eds. Cambridge University Press, 1217–1308.

Colle, B. A., Zhang, Z., Lombardo, K. A., Chang, E., Liu, P., and Zhang, M., 2013: Historical evaluation and future prediction of eastern North American and western Atlantic extratropical cyclones in the CMIP5 models during the cool season. *J. Climate*, **26(18)**, 6882-6903, https://doi.org/10.1175/JCLI-D-12-00498.1.

Delworth, T. L., and Coauthors, 2020: SPEAR: The next generation GFDL modeling system for seasonal to multidecadal prediction and projection. *J. Adv. Model. Earth Syst.*, **12(3)**, e2019MS001895, https://doi.org/10.1029/2019MS001895.

Earl, N., Dorling, S., Starks, M. and Finch, R., 2017: Subsynoptic-scale features associated with extreme surface gusts in UK extratropical cyclone events. *Geophys. Res. Lett.*, **44**, 3932-3940. https://doi.org/10.1002/2017GL073124.

Gentile, E. S., Zhao, M., and Hodges, K., 2023: Poleward intensification of midlatitude extreme winds under warmer climate. *npj Climate Atmos. Sci.*, **6**, 219, https://doi.org/10.1038/s41612-023-00540-x.

Haarsma, R. J., and Coauthors, 2016: High resolution model intercomparison project (HighResMIP v1. 0) for CMIP6. *Geosci. Model Dev.*, **9(11)**, 4185-4208, https://doi.org/10.5194/gmd-9-4185-2016.

Hart, N.C.G., Gray, S.L. and Clark, P.A., 2017: Sting-jet windstorms over the North Atlantic: climatology and contribution to extreme wind risk. *J. Climate*, **30**, 5455-5471. https://doi.org/10.1175/JCLI-D-16-0791.1.

Harvey, B. J., Cook, P., Shaffrey, L. C., and Schiemann, R., 2020: The response of the northern hemisphere storm tracks and jet streams to climate change in the CMIP3,

Accepted for publication in *Journal of Climate.* DOI 10.1175/JCLI-D-24-0770.1.

CMIP5, and CMIP6 climate models. *J. Geophys. Res.: Atmos.*, **125(23)**, e2020JD032701. https://doi.org/10.1029/2020JD032701.

Hawcroft, M. K., Shaffrey, L. C., Hodges, K. I., and Dacre, H. F., 2012: How much Northern Hemisphere precipitation is associated with extratropical cyclones?. *Geophys. Res. Lett.*, **39(24)**, https://doi.org/10.1029/2012GL053866.

Hersbach, H., and Coauthors, 2020: The ERA5 global reanalysis. *Quart. J. Roy. Meteor. Soc.*, **146(730)**, 1999-2049, https://doi.org/10.1002/qj.3803.

Hewson, T.D. and Neu, U., 2015: Cyclones, windstorms and the IMILAST project. *Tellus A*, **67**, 27-128. https://doi.org/10.3402/tellusa.v67.27128.

Hodges, K. I., 1994: A general method for tracking analysis and its application to meteorological data. *Mon. Wea. Rev.*, **122**, 2573–2586, https://doi.org/10.1175/1520-0493(1994)122<2573:agmfta>2.0.co;2.

Hodges, K. I., 1995: Feature tracking on the unit sphere. *Mon. Wea. Rev.*, **123**, 3458–3465, https://doi.org/10.1175/1520-0493(1995)123<3458:ftotus>2.0.co;2.

Hodges, K. I., 1999: Adaptive constraints for feature tracking. *Mon. Wea. Rev.*, **127**, 1362–1373. https://doi.org/10.1175/1520-0493(1999)127<1362:acfft>2.0.co;2.

Hodges, K. I., Hoskins, B. J., Boyle, J., and Thorncroft, C., 2003: A comparison of recent reanalysis datasets using objective feature tracking: Storm tracks and tropical easterly waves. *Mon. Wea. Rev.*, **131(9)**, 2012-2037, https://doi.org/10.1175/1520-0493(2003)131<2012:ACORRD>2.0.CO;2.

Hoskins, B. J., and Hodges, K. I., 2002: New perspectives on the Northern Hemisphere winter storm tracks. *J. Atmos. Sci.*, **59(6)**, 1041-1061, https://doi.org/10.1175/1520-0469(2002)059<1041:NPOTNH>2.0.CO;2.

Jiaxiang, G., and Coauthors, 2020: Influence of model resolution on bomb cyclones revealed by HighResMIP-PRIMAVERA simulations. *Environ. Res. Lett.*, **15(8)**, 084001, https://doi.org/10.1088/1748-9326/ab88fa.

Jong, B. T., Delworth, T. L., Cooke, W. F., Tseng, K. C., and Murakami, H., 2023: Increases in extreme precipitation over the Northeast United States using high-resolution climate model simulations. *npj Climate Atmos. Sci.*, **6(1)**, 18, https://www.nature.com/articles/s41612-023-00347-w.

Jong, B., H. Murakami, T. L. Delworth, and W. Cooke, 2024: Contributions of tropical cyclones and atmospheric rivers to extreme precipitation trends over the Northeast US. *Earth's Future,* **12,** e2023EF004370, http://dx.doi.org/10.1029/2023EF004370.

Jung, T., Gulev, S. K., Rudeva, I., and Soloviov, V., 2006: Sensitivity of extratropical cyclone characteristics to horizontal resolution in the ECMWF model. *Quart. J. Roy. Meteor. Soc.*, **132(619)**, 1839-1857, https://doi.org/10.1256/qj.05.212.

Kang, J. M., Lee, J., Son, S. W., Kim, J., and Chen, D., 2020: The rapid intensification of East Asian cyclones around the Korean Peninsula and their surface impacts. *J. Geophys. Res.: Atmos.*, **125(2)**, e2019JD031632, https://doi.org/10.1029/2019JD031632.

Kaspi, Y., and Schneider, T., 2013: The role of stationary eddies in shaping midlatitude storm tracks. *J. Atmos. Sci.*, **70(8)**, 2596–2613, https://doi.org/10.1175/JAS-D-12-082.1.

Kosaka, Y., and Coauthors, 2024: The JRA-3Q reanalysis. *J. Meteor. Soc. Japan. Ser. II*, **102(1)**, 49-109, https://doi.org/10.2151/jmsj.2024-004.

Kohonen, T., 1998: The self-organizing map. *Neurocomputing*, **21**, 1–6, https://doi.org/10.1016/S0925-2312(98)00030-7.

Kohonen, T., 2013: Essentials of the self-organizing map. *Neural networks*, **37**, 52–65, https://doi.org/10.1016/j.neunet.2012.09.018.

Li, J., Zhao, Y., Chen, D., Zhao, P., Zhang, C., and Wang, Y., 2024: The quantitative role of moisture and vertical motion in shaping summer heavy rainfall over North China under two distinct large-scale weather patterns. *J. Climate*, **37(8)**, 2655-2672, https://doi.org/10.1175/JCLI-D-22-0850.1.

Ludwig, P., Pinto, J. G., Hoepp, S. A., Fink, A. H., and Gray, S. L., 2015: Secondary cyclogenesis along an occluded front leading to damaging wind gusts: Windstorm Kyrill, January 2007. *Mon. Wea. Rev.*, **143(4)**, 1417-1437, https://doi.org/10.1175/MWR-D-14-00304.1.

Messmer, M., and Simmonds, I., 2021: Global analysis of cyclone-induced compound precipitation and wind extreme events. *Wea. Climate Extremes*, **32**, 100324, https://doi.org/10.1016/j.wace.2021.100324.

Murakami, H., Delworth, T. L., Cooke, W. F., Zhao, M., Xiang, B., and Hsu, P. C., 2020: Detected climatic change in global distribution of tropical cyclones. *Proc. Natl. Acad. Sci.*, **117(20)**, 10706-10714, https://doi.org/10.1073/pnas.1922500117.

Murakami, H., W. Cooke, R. Mizuta, H. Endo, K. Yoshida, S. Wang, and P. Hsu, 2024a: Robust future projections of global spatial distribution of major tropical cyclones and sea level pressure gradients. *Commun. Earth Environ.*, **5,** 479, http://dx.doi.org/10.1038/s43247-024-01644-9.

Murakami, H., 2024: Effect of regional anthropogenic aerosols on tropical cyclone frequency of occurrence. *Geophys. Res. Lett.*, **51,** e2024GL110443, http://dx.doi.org/10.1029/2024GL110443.

Neu, U., and Coauthors, 2013: IMILAST: A community effort to intercompare extratropical cyclone detection and tracking algorithms. *Bull. Amer. Meteor. Soc.*, **94**, 529–547, https://doi.org/10.1175/BAMS-D-11-00154.1.

Pinto, J. G., Bellenbaum, N., Karremann, M. K., and Della-Marta, P. M., 2013: Serial clustering of extratropical cyclones over the North Atlantic and Europe under recent and future climate conditions. *J. Geophys. Res.: Atmos.*, **118(22)**, 12-476, https://doi.org/10.1002/2013JD020564.

Priestley, M. D., Ackerley, D., Catto, J. L., Hodges, K. I., McDonald, R. E., and Lee, R. W., 2020a: An overview of the extratropical storm tracks in CMIP6 historical simulations. *J. Climate*, **33(15)**, 6315-6343, https://doi.org/10.1175/JCLI-D-19-0928.1.

Priestley, M. D., and Catto, J. L., 2022: Improved representation of extratropical cyclone structure in HighResMIP models. *Geophys. Res. Lett.*, **49(5)**, e2021GL096708, https://doi.org/10.1029/2021GL096708.

Priestley, M. D., Dacre, H. F., Shaffrey, L. C., Schemm, S., and Pinto, J. G., 2020b: The role of secondary cyclones and cyclone families for the North Atlantic storm track and clustering over western Europe. *Quart. J. Roy. Meteor. Soc.*, **146(728)**, 1184-1205, https://doi.org/10.1002/qj.3733.

Reusch, D. B., Alley, R. B., and Hewitson, B. C., 2005: Relative performance of self-organizing maps and principal component analysis in pattern extraction from synthetic climatological data. *Polar geogr.*, **29(3)**, 188-212, https://doi.org/10.1080/789610199.

Rivals, H., Cammas, J. P., and Renfrew, I. A., 1998: Secondary cyclogenesis: The initiation phase of a frontal wave observed over the eastern Atlantic. *Quart. J. Roy. Meteor. Soc.*, **124(545)**, 243-267, https://doi.org/10.1002/qj.49712454511.

Rohrer, M., Martius, O., Raible, C. C., and Brönnimann, S., 2020: Sensitivity of blocks and cyclones in ERA5 to spatial resolution and definition. *Geophys. Res. Lett.*, **47(7)**, e2019GL085582, https://doi.org/10.1029/2019GL085582.

Rudeva, I., and Gulev, S. K., 2007: Climatology of cyclone size characteristics and their changes during the cyclone life cycle. *Mon. Wea. Rev.*, **135(7)**, 2568-2587, https://doi.org/10.1175/MWR3420.1.

Schemm, S., and Sprenger, M., 2015: Frontal-wave cyclogenesis in the North Atlantic–a climatological characterisation. *Quart. J. Roy. Meteor. Soc.*, **141(693)**, 2989-3005, https://doi.org/10.1002/qj.2584.

Schemm, S., 2023: Toward Eliminating the Decades-Old "Too Zonal and Too Equatorward" Storm-Track Bias in Climate Models., *J. Adv. Model. Earth Syst.*, **15**, e2022MS003482, https://doi.org/10.1029/2022MS003482.

Seiler, C., and Zwiers, F. W., 2016: How well do CMIP5 climate models reproduce explosive cyclones in the extratropics of the Northern Hemisphere?. *Climate Dyn.*, **46(3-4)**, 1241-1256, https://doi.org/10.1007/s00382-015-2642-x.

Small, R. J., Msadek, R., Kwon, Y-O., Booth J., and Zarzycki C., 2019: Atmosphere surface storm track response to resolved ocean mesoscale in two sets of global climate model experiments. *Climate Dyn.*, **52**, 2067–2089, https://doi.org/10.1007/s00382-018-4237-9.

Tseng, K.-C., and Coauthors, 2021: Are multiseasonal forecasts of atmospheric rivers possible?, *Geophys. Res. Lett.*, **48**, e2021GL094000, https://doi.org/10.1029/2021GL094000.

Vettigli, G., 2021: MiniSom. Accessed 10 May 2022, https://github.com/JustGlowing/minisom.

Wang, S., H. Murakami, and W. F. Cooke, 2023: Anthropogenic forcing changes coastal tropical cyclone frequency. *npj Climate Atmos. Sci.*, **6,** 187, http://dx.doi.org/10.1038/s41612-023-00537-x.

Wang, S., H. Murakami, and W. F. Cooke, 2024: Anthropogenic effects on tropical cyclones near western Europe. *npj Climate Atmos. Sci.*, **7,** 173, http://dx.doi.org/10.1038/s41612-024-00721-2.

Wernli, H., and Davies, H. C., 1997: A Lagrangian-based analysis of extratropical cyclones. I: The method and some applications. *Quart. J. Roy. Meteor. Soc.*, **123(538)**, 467-489, https://doi.org/10.1002/qj.49712353811.

Willison, J., Robinson, W. A., and Lackmann, G. M., 2013: The importance of resolving mesoscale latent heating in the North Atlantic storm track. *J. Atmos. Sci.*, **70(7)**, 2234-2250, https://doi.org/10.1175/JAS-D-12-0226.1.

Woollings, T., Hoskins, B., Blackburn, M., Hassell, D., and Hodges, K., 2010: Storm track sensitivity to sea surface temperature resolution in a regional atmosphere model. *Climate Dyn.*, **35**, 341-353, https://doi.org/10.1007/s00382-009-0554-3.

Yang, X., Delworth, T. L., Jia, L., Johnson, N. C., Lu, F., and McHugh, C., 2022: On the seasonal prediction and predictability of winter surface Temperature Swing Index over North America. *Front. Climate*, **4**, 972119, https://doi.org/10.3389/fclim.2022.972119.

Yun, Y., Zeng, Q., Green, B. W., and Zhang, F., 2015: Mitigating atmospheric effects in InSAR measurements through high-resolution data assimilation and numerical simulations with a weather prediction model. *Int. J. Remote Sens.*, **36(8)**, 2129-2147, https://doi.org/10.1080/01431161.2015.1034894.

Zappa, G., Shaffrey, L. C., and Hodges, K. I., 2013: The ability of CMIP5 models to simulate North Atlantic extratropical cyclones. *J. Climate*, **26(15)**, 5379-5396, https://doi.org/10.1175/JCLI-D-12-00501.1.

Zhang, G., and Coauthors, 2021: Seasonal predictability of baroclinic wave activity. *npj Climate Atmos. Sci.*, **4(1)**, 50, https://doi.org/10.1038/s41612-021-00209-3.

Zhao, M., and Coauthors, 2018a: The GFDL global atmosphere and land model AM4. 0/LM4. 0: 1. Simulation characteristics with prescribed SSTs. *J. Adv. Model. Earth Syst.*, **10(3)**, 691-734, https://doi.org/10.1002/2017MS001208.

Zhao, M., and Coauthors, 2018b: The GFDL global atmosphere and land model AM4. 0/LM4. 0: 2. Model description, sensitivity studies, and tuning strategies. *J. Adv. Model. Earth Syst.*, **10(3)**, 735-769. https://doi.org/10.1002/2017MS001209.

Accepted for publication in *Journal of Climate.* DOI 10.1175/JCLI-D-24-0770.1.